HHS Public Access

Author manuscript

Brain Res. Author manuscript; available in PMC 2020 August 15.

Published in final edited form as:

Brain Res. 2019 August 15; 1717: 147–159. doi:10.1016/j.brainres.2019.04.015.

CELL BASED THERAPY REDUCES SECONDARY DAMAGE AND INCREASES EXTENT OF MICROGLIAL ACTIVATION FOLLOWING CORTICAL INJURY

Mary E. Orczykowski[a,1], **Samantha M. Calderazzo**[a], **Eli Shobin**[a], **Monica A Pessina**[a], **Adrian L. Oblak**[a,2], **Seth P. Finklestein**[d], **Brian C. Kramer**[e], **Farzad Mortazavi**[a], **Douglas L. Rosene**[a,b], and **Tara L. Moore**[a,c]

[a]Department of Anatomy & Neurobiology, 72 E. Concord Street, L-1004, Boston University School of Medicine, Boston, MA USA 02118

[b]Yerkes National Primate Research Center, 201 Dowman Drive, Emory University, Atlanta, GA, USA 30322

[c]Department of Neurology, 72 E. Concord Street, C3, Boston University School of Medicine, Boston, MA USA 02118

[d]Stemetix, Inc, 604 Webster St., Needham, MA 02494

[e]Janssen Scientific Affairs, LLC, 800 Ridgeview Drive, Horsham, PA 19044

Abstract

Cortical injury elicits long-term cytotoxic and cytoprotective mechanisms within the brain and the balance of these pathways can determine the functional outcome for the individual. Cytotoxicity is exacerbated by production of reactive oxygen species, accumulation of iron, and peroxidation of cell membranes and myelin. There are currently no neurorestorative treatments to aid in balancing the cytotoxic and cytoprotective mechanisms following cortical injury. Cell based therapies are an emerging treatment that may function in immunomodul ation, reduction of secondary damage, and reorganization of surviving structures. We previously evaluated human umbilical tissue-derived cells (hUTC) in our non-human primate model of cortical injury restricted to the hand area of primary motor cortex. Systemic hUTC treatment resulted in significantly greater recovery of fine motor function compared to vehicle controls. Here we investigate the hypothesis that hUTC treatment reduces oxidative damage and iron accumulation and increases the extent of the microglial response to cortical injury. To test this, brain sections from these monkeys were processed using immunohistochemistry to quantify oxidative damage (4-HNE) and activated microglia (LN3), and Prussian Blue to quantify iron. hUTC treated subjects exhibited significantly reduced oxidative damage in the sublesional white matter and iron accumulation in the perilesional

Corresponding Author: Mary Orczykowski, Division of Anatomical Sciences, University of Michigan Medical School, Ann Arbor, MI 48109, contact: meorcz@umich.edu or mary.orczykowski@gmail.com.

[1]Present Address: Division of Anatomical Sciences, University of Michigan Medical School, Ann Arbor, MI 48109

[2]Present Address: Department of Pathology and Laboratory Medicine, Indiana University School of Medicine, Indianapolis, IN 46202

area as well as a significant increase in the extent of activated microglia along white matter pathways. Increased perilesional iron accumulation was associated with greater perilesional oxidative damage and larger reconstructed lesion volume. These findings support the hypothesis that systemic hUTC administered 24 hours after cortical damage decreases the cytotoxic response while increasing the extent of microglial activation.

Keywords

Cell Based Therapy; hUTC3; Cortical Damage; Secondary Damage; Oxidative Stress; Microglia

1. INTRODUCTION

Cell based therapies are potential neurorestorative treatments for cortical injury that have shown promising results in preclinical studies. While the mechanism of these therapies remains unclear, rodent studies suggest that cell based therapies modulate post-injury inflammation and reduce resulting secondary damage (Savitz et al., 2014). To further explore cell therapies as a treatment for cortical injury, we previously assessed a cell based therapy containing human umbilical tissue-derived cells (hUTC) in our non-human primate model of cortical injury. We found that intravenous administration of hUTC, 24 hours after cortical damage, significantly improved fine motor function and strength of the impaired hand in the first two weeks of recovery as well as improved finger-thumb grasp over the 12-week post operative assessment compared to vehicle treated controls (Moore et al., 2013).

Metabolic stress following cortical injury such as ischemic stroke leads to neuronal death, accumulation of reactive oxygen species (ROS), disruption of iron homeostasis, and recruitment of immune cells (Lipton, 1999). Excess ROS both intra- and extracellularly in the area of ischemia leads to further necrosis via lipid peroxidation in the ischemic core and apoptosis in neighboring neurons (Brouns and De Deyn, 2009). Lipid peroxidation is further catalyzed by the presence of unbound iron (Gutteridge, 2006). Following ischemic injury, iron homeostasis is disrupted resulting in an increase of total brain iron and leading to further neuronal damage (Selim and Ratan, 2004). The Fenton reaction and Haber-Weiss cycle perpetuate this disruption in iron homeostasis thus producing an increasing pool of hydroxyl free radicals (Winterbourn, 1995). Hydroxyl free radicals initiate lipid peroxidation and other oxidative damage in the area of ischemia (Bresgen and Eckl, 2015). At the same time, microglia contribute to both the resolution of inflammation and perpetuation of secondary damage following cortical injury (Kreutzberg, 1996). Studies assessing cell therapy treatments similar to hUTC infusion have observed an immunomodulatory effect (Calio et al., 2014; Fumagalli et al., 2015; Satani and Savitz, 2016). Specifically, cell therapy is associated with a reduction in oxidative stress (Calio et al., 2014) and polarization of microglia and macrophages to a protective phenotype leading to an improved functional outcome (Fumagalli et al., 2015; Ohtaki et al., 2008). Therefore, we hypothesized that hUTC infusion enhances the microglial response and reduces cytotoxic responses to cortical injury by interrupting the cycle of ROS production and subsequent oxidative stress.

In order to investigate this hypothesized effect of hUTC treatment, we processed brain tissue sections from both hUTC and vehicle treated monkeys to assess the effect on inflammatory processes and secondary damage that occurs after injury. Specifically, here we examined and quantified markers of oxidative damage, iron, and activated microglia in brain tissue harvested 14 weeks after injury in hUTC treated and vehicle treated monkeys evaluated for recovery of function.

2. RESULTS

2.1 Effect of hUTC on Oxidative Damage

Following lipid peroxidation of cell membranes, both 4-hydroxynonenal (4-HNE) and malondialdehyde (MDA) remain in the tissue as evidence of oxidative damage. The level of lipid peroxidation was evaluated with 4-HNE immunohistochemistry. 4-HNE staining was localized to the area of the lesion (Figure 1A). Regions of interest (ROI) for 4-HNE densitometry included perilesional gray matter (PLG) and sublesional white matter (SLW). PLG was external to the gray-white boundary and extended medially toward the cingulate sulcus and laterally toward the circular sulcus. SLW extends from the gray-white boundary to a line between the cingulate and circular sulci. Refer to Figure 9 and Section 4.4 for details. Levels of 4-HNE staining were significantly lower in the sublesional white matter with hUTC treatment (p=0.033; Figure 1B). However, levels of 4-HNE did not differ in the perilesional gray matter between groups (p= 0.169). These results suggest that while both groups had high levels of oxidative damage from the initial lesion, hUTC treated monkeys had a lower accumulation of oxidative damage in the sublesional white matter compared to vehicle controls.

2.2 Effect of hUTC on Iron Accumulation

On gross inspection of the brain, the composition of the lesion differed between groups in that the lesion area of the vehicle monkeys was much darker in appearance than in the hUTC treated monkeys as shown in Figure 2A–B. The Prussian Blue staining method was used to evaluate this as Prussian Blue catalyzes blue pigment accumulation in areas of iron. While a baseline amount of iron is expected in the brain, areas of aggregation represent pathological iron accumulations such as hemosiderin. As shown in Figure 2C, Prussian Blue staining differed between vehicle and hUTC treated subjects. To quantify this, we evaluated the total volume stained with Prussian Blue in the perilesional area, the thresholded percent area stained, and the optical density (intensity) of staining. The ROI was defined as the extent of Prussian Blue staining adjacent the lesion to its medial and lateral boundaries and as deep into the white matter as the dark blue staining extended. Refer to Figure 9 and Section 4.4 for details. As shown in Figure 2D, the total volume (mm^3) of the lesion with Prussian Blue staining was not significantly different (p = 0.416, Figure 2D). However, the percent area of Prussian Blue staining above a consistent threshold was significantly lower in the lesion area following hUTC treatment (p = 0.045; Figure 2E). Furthermore, the intensity of Prussian Blue staining was significantly lower with hUTC treatment (p = 0.002; Figure 2F). These results suggest that the amount and concentration of iron accumulated in the area of the lesion was lower in hUTC treated monkeys compared to vehicle controls.

2.3 Effect of hUTC on Density of Activated Microglia in Perilesional Gray and Sublesional White Matter

Activated microglia were identified using immunohistochemistry and the LN3 antibody, which is a marker for MHC-II. Accumulations of LN3 positive microglia were present in the area of the lesion. The density of activated microglia in the perilesional gray matter and sublesional white matter was estimated using unbiased stereology and the Cavalieri volume estimation. Density (cells/mm^3) was used in order to control for the variance in total volume of each ROI. ROIs were determined using the same boundaries as for 4-HNE densitometry. Refer to Figure 9 and Section 4.4 for details. The total density of activated microglia approached a significant increase in the perilesional gray matter (p =0.071) and the sublesional white matter (p =0.093) (Figure 3) with hUTC treatment.

2.4 Effect of hUTC on Morphology of Activated Microglia in Perilesional Gray and Sublesional White Matter

While MHC-II positive microglia imply a readiness to respond to antigen presentation, we further assessed microglia by morphology to identify ramified, hypertrophic, or amoeboid using previously published studies (Karperien et al., 2013; Shobin et al., 2017) as a guide. Examples of these morphological criteria for our LN3 positive microglia are shown in Figure 4. Ramified microglia included a small, well-defined cell body and thin processes (Figure 4A) and were representative of a surveilling phenotype. Hypertrophic microglia presented with either a small cell body and thick retracted processes or a large cell body with thin processes (Figure 4B) and represent a transition state of de-ramifying or re-ramifying. Amoeboid microglia had thick retracted processes or no processes extending from an enlarged cell body (Figure 4C) and represent mobile, phagocytic cells.

All microglial morphologies (ramified, hypertrophic, and amoeboid) were present in lesion area including both the perilesional gray and sublesional white matter. Stereological analysis revealed a significant difference in the density (cells/mm^3) of specific microglial morphologies in the perilesional gray matter [$F_{(1,6)} = 9.108$, $p = 0.004$], but no significant difference between groups [$F_{(1,6)} = 2.87$, $p = 0.141$] or interaction with group differences (Figure 4D). Similarly, there is a significant difference in density by morphology in sublesional white matter [$F_{(1,6)}= 26.307$, $p = 0.0004$], but no significant difference between groups [$F_{(1,6)} = 2.24$, $p = 0.185$] or interaction with group differences (Figure 4E). However, hUTC treated monkeys had a consistently higher number of all morphologies in both the perilesional gray matter and sublesional white matter suggesting an overall increase in the extent of microglial activation.

2.5 Effect of hUTC on Extent of Activated Microglia

Activated microglia were extensively present in the lesion area as described above but in addition they also radiated from the lesion territory out along white matter pathways (Figure 5). To quantify the level of staining in these areas, visual ratings between 0 (no staining) and 4 (intense staining) were given to specific regions of the cortical gray matter and white matter pathways on blinded LN3 stained sections from each subject. Activated microglia were heavily present around the lesion in the ipsilesional primary motor cortex equally in both treated (2.34) and vehicle (2.44) monkeys (Figure 6A). Similarly, minimal staining was

found in contralesional primary motor cortex in both treated (0.10) and vehicle (0.20) monkeys. Staining was present in white matter pathways with ratings ranging from 1.1 to 2.9 in both hUTC and vehicle monkeys, specifically in corpus callosum as well as ipsilesional frontal white matter, internal capsule, and cerebral peduncle. Interestingly, staining was also present in ipsilesional and contralesional temporal lobe white matter in both treated and vehicle monkeys. Staining intensity was significantly higher in hUTC treated monkeys in the contralesional frontal white matter ($p = 0.021$) and contralesional temporal lobe white matter ($p = 0.037$) compared to vehicle controls (Figure 6A). Overall, there was a stronger intensity of activated microglia in white matter pathways with hUTC treatment.

To further quantify the extent of LN3 staining, sections containing both ipsilesional and contralesional hemispheres with regions scoring 2, 3, or 4 (medium to intense staining) were outlined and total gray and white matter volumes were measured. There is a trend toward a greater extent of LN3 staining in gray matter areas (primary motor, ventral and dorsal premotor cortices, and somatosensory) with hUTC treatment ($p = 0.066$) (Figure 6B). Further, there is a greater extent of LN3 staining in white matter pathways with hUTC treatment ($p = 0.042$) (Figure 6C). These results suggest that there is an increased extent of microglial activation with hUTC treatment in white matter pathways.

2.6 Relationship Between Oxidative Damage, Iron Accumulation, Activated Microglia, and Lesion Volume

Since monkeys in both hUTC treatment and vehicle groups showed some recovery with hUTC treatment enhancing the endogenous recovery mechanisms, we applied a regression analyses to the pooled group of all subjects (n = 8) to explore the relationships among the brain tissue variables measured here and reconstructed lesion volume from our previous study (Moore et al., 2013).

Based on the known interaction between iron and lipid peroxidation (Bresgen and Eckl, 2015; Winterbourn, 1995), we hypothesized that our results of 4-HNE and Prussian Blue staining in the lesion area would be correlated. Further, we hypothesized that the density of amoeboid (phagocytic) microglia will predict the levels of oxidative damage and iron. There was a strong positive correlation between the volume of iron accumulation and oxidative damage in the perilesional gray matter (R_p (6) = 0.898 and $p = 0.002$, Figure 7A). However, there was no significant correlation between amoeboid microglia and 4-HNE in the perilesional gray matter (R_p (6) = 0.237 and $p = 0.572$) or in the sublesional white matter (R_p (6) = 0.430 and $p = 0.288$). Further, there was no correlation between amoeboid microglia and volume of iron accumulation in the perilesional gray matter (R_p (6) = 0.547 and $p = 0.160$), which may be due to the 14 week time point assessed in this study. These results suggest that the presence of iron increased the formation of ROS and lipid peroxidation.

As previously reported, there was no group difference between hUTC treated and vehicle control monkeys in lesion volume (cortex lost) reconstructed from Nissl stained sections (Moore et al., 2013). However, there was a positive linear relationship between reconstructed lesion volume and the volume of iron accumulation (affected cortex) (R_p (6) = 0.771 and $p =$

0.048, Figure 7B). Further, there was a trend toward a correlation between reconstructed lesion volume and density of amoeboid microglia in the perilesional gray matter (R_p (6) = 0.662 and p = 0.074). Finally, there was no significant correlation with reconstructed lesion volume and perilesional 4-HNE (R_p (6) = 0.581 and p = 0.130). These results suggest that iron accumulation may increase lesion area via secondary damage in terms of cortex lost and result in greater activation of amoeboid microglia.

3. DISCUSSION

3.1 Summary

In this study, we tested the hypothesis that systemic hUTC infusion affects the microglial response and reduces cytotoxic responses to cortical injury, by interrupting the cycle of ROS production and oxidative stress. To our knowledge, this is the first study to investigate the relationship of oxidative damage, iron homeostasis, and activated microglia following cortical injury with a cell based therapy. The overall findings of this study are: (1) Oxidative damage is lower in the sublesional white matter with hUTC treatment. (2) The amount and concentration of perilesional iron accumulation is lower with hUTC treatment. (3) The extent and volume of microglial activation is significantly higher in the white matter areas of hUTC treated monkeys compared to vehicle controls. (4) Lesion volume and perilesional oxidative damage are associated with perilesional iron accumulation. Overall, these results suggest that systemic hUTC infusion may reduce secondary damage and increase recruitment of microglia following cortical injury.

3.2 Oxidative Stress Following Cortical Injury

It is well established that metabolic crisis following cortical injury, such as stroke, leads to an increase in ROS and oxidative stress (Fumagalli et al., 2015). The source of ROS is either through the destruction of cells undergoing oxidative stress, thus releasing ROS, or through the release of ROS from classically activated microglia or macrophages (Amantea et al., 2015). As a consequence of ROS accumulation, lipid peroxidation breaks down both cell membranes and myelin resulting in the production of 4-hydroxynonenal (4-HNE) and malondialdyde (MDA) (Mimica-Duki et al., 2012; Ravera et al., 2015; Selim and Ratan, 2004). Reduced initial ROS accumulation leads to a reduction in residual damage and neuronal death (Navarro-Yepes et al., 2014; Rana and Singh, 2018). Transplantation of mesenchymal stem cells (MSC) in an aged model of stroke led to a reduction of oxidative damage (Calio et al. 2014). In this study, we measured the level of 4-HNE using immunohistochemistry and semi- quantitative analysis. We observed reduced 4-HNE in the sublesional white matter with hUTC treatment, suggesting hUTC prevent the accumulation of ROS and resulting oxidative damage.

3.3 Iron Homeostasis Disruption

Following cortical injury, total brain iron concentration increases and ferric iron disassociates with its binding proteins, transferrin and ferritin, due to an acidic environment or by lysosomal degradation (Lipton, 1999; Selim and Ratan, 2004). The expanding pool of dissociated and free iron catalyzes formation of ROS (Selim and Ratan, 2004). Further, ferritin accumulates with cellular debris forming the protein aggregate, hemosiderin, which

binds ferric iron, rendering it poorly available (Gutteridge and Hou, 1986). Further, studies suggest that iron neurotoxicity is associated with a larger lesion following stroke (Demougeot et al., 2004; Selim and Ratan, 2004). While many studies use superparamagnetic iron oxide nanoparticles to track cell based therapies using imaging techniques, to our knowledge, no other study has yet quantified iron accumulation in relation to recovery from cortical injury and cell based therapies. In this study, we used Prussian Blue histology to quantify the amount and concentration of iron accumulation in the cortical area surrounding the lesion and we found reduced iron concentration with hUTC treatment. In addition, although studies assessing hUTC therapy have consistently reported no change in reconstructed lesion volume (cortex lost) (Moore et al., 2013; Shams Ara et al., 2015; Shehadah et al., 2013; Yang et al., 2012; Zhang et al., 2013, 2012, 2011), our results reveal that reconstructed lesion volume was larger with increased volume of perilesional iron volume. Our previous study showed evidence of cortical reorganization with hUTC treatment in this model (Orczykowski et al., 2018), so we propose that the treatment induced reduction in iron and oxidative damage in our model may have reduced secondary injury and enabled more effective reorganization rather than reducing reconstructed lesion volume.

3.4 The Relationship Between Oxidative Stress and Iron

The positive feedback between unbound iron and ROS is well documented in its contribution to neuronal damage following stroke (Minotti and Aust, 1989; Selim and Ratan, 2004). Initially, lipids are peroxidized in the presence of ROS. Then, unbound reactive ferrous iron reduces any peroxides into hydroxyl free radicals and ferric iron. While ferric iron is more stable, it lends its electron to neutralize the abundant ROS present after injury, thus returning to ferrous iron. The Fenton and Haber-Weiss Reactions perpetuate this cycle, disturbing the homeostasis of iron and producing an increasing pool of ROS (Winterbourn, 1995). Free radicals may then contribute to the initiation of further lipid peroxidation and other oxidative damage in the area of ischemia (Bresgen and Eckl, 2015). Our results show that perilesional oxidative damage increases with increasing perilesional iron accumulation. Based on the literature and our findings, we propose that interrupting the cycle of iron and ROS interaction may reduce overall damage accumulation and neurotoxicity in the lesion area. Relevant mechanisms are summarized in Figure 8.

3.5 Microglia in Acute Inflammation and Resolution of Cortical Injury

In homeostasis, microglia (ramified or rod-like) are motile, non-migratory, and morphologically plastic, remaining primed to respond quickly to changes in the environment (Eyo and Dailey, 2013; Kreutzberg, 1996). Following injury, microglia are the first responders in the CNS (Patel et al., 2013), undergoing a differential activation and homing to the site of injury through chemotaxis (Fumagalli et al., 2015; Kreutzberg, 1996). Microglia contribute to both the resolution of inflammation and perpetuation of secondary damage following cortical injury (Kreutzberg, 1996). The activation and phenotypic switch of microglia following injury has been shown to have a temporal pattern of expression (Perego et al., 2011). In the acute phase, classically activated microglia and macrophages in this area localize to the area of a lesion through signals from neurons undergoing metabolic stress leading to apoptosis and necrosis. Classically activated microglia and macrophages promote neurotoxicity through the release of pro-inflammatory cytokines, proteases, and ROS (Patel

et al., 2013). It remains unclear how inflammation converts to resolution and neuroprotective processes following cortical injury (Shichita et al., 2014). However, throughout resolution of inflammatory events, microglia and macrophages polarize from classically to alternatively activated phenotypes through environmental signals (Fumagalli et al., 2015). In alternative activation, microglia secrete growth factors and anti-inflammatory cytokines promoting lesion repair and removal of cell debris (Fumagalli et al., 2015; Patel et al., 2013).

In the present study, activated microglia were quantified using immunohistochemistry, stereology, and densitometry. The marker used for microglia was MHC Class II (HLA-DR) and represents reactivity, but does not further differentiate these cells between peripheral macrophages and microglia or whether they were classically or alternatively activated (London et al., 2013). Therefore, we further quantified activated microglia by morphology (ramified, hypertrophic, and amoeboid) to elucidate their functional phenotype (Karperien et al., 2013; Shobin et al., 2017). While our results showed no significant difference in density of microglia with hUTC treatment, the density of all phenotypes was higher in treated monkeys compared to vehicle controls suggesting greater widespread microglial activation with treatment. Studies observed that microglia near the penumbra may be neuroprotective and enhance plasticity through the release of neurotrophic factors (Anttila et al., 2016; Lalancette-Hebert et al., 2007; Liguz-Lecznar and Kossut, 2013; Narantuya et al., 2010). Further, studies assessing cell based therapy after cortical injury observed increased cytoprotective microglia and reduced cytotoxic microglia in the lesion area (Yoo et al., 2013; Zanier et al., 2014, 2011). We propose that widespread activation of microglia may have been protective leading to effective clearing of debris and enhanced plasticity in the perilesional area. However, future studies are needed to clarify exact changes in the genetic expression profiles of microglia and macrophages influenced by cell based therapies *in vivo* and to validate the relationship of morphology to functional phenotype.

3.6 White Matter Repair Following Cortical Injury

Both cell death and white matter disruption contribute to functional deficits observed after brain injury. Following pathological events, microglia remove myelin debris, which in excess prevents effective remyelination (Lampron et al., 2015) and can eliminate synapses and assist in guiding neurite outgrowth (Eyo and Dailey, 2013). Further, microglia aid in white matter repair after stroke (Jiang et al., 2016). In the current study, we observe lower levels of oxidative damage in sublesional white matter and a marked increase in the extent of microglial activation in the white matter areas following hUTC treatment. We propose that the increase in the extent of microglial activation could have led to a reduction in myelin degradation and oxidative damage in sublesional white matter and more effective remyelination and repair in white matter pathways.

3.7 Potential of Cell Based Therapy

Studies assessing cell based therapies corroborate the hypothesis that paracrine signals from the cell therapy modulate the inflammatory response to ischemia (Fumagalli et al., 2015), reduce secondary damage (Calio et al., 2014; Chen et al., 2016; Shams Ara et al., 2015; Zhang et al., 2012, 2011), and enhance reorganization of surviving structures (Arbab et al., 2012; Jiang et al., 2012; Koh et al., 2018, 2015; Shehadah et al., 2013; Yang et al., 2012;

Zhang et al., 2013, 2012, 2011). Following intravenous injection, hUTC return to the heart then enter and congregate in the lungs, liver, and spleen (Arbab et al., 2012). Exogenous cell based therapies migrating to the spleen within days of injury onset may allow for peripheral immune modulation through the spleen (Arbab et al., 2012; Yang et al., 2017; Yoon et al., 2010). While spleen modulation by hUTC following cortical injury has yet to be directly assessed, a study that injected bone marrow mesenchymal stem cells intravenously following stroke found downregulated immune activation genes in splenocytes, upregulated serum expression of anti-inflammatory cytokines (IL-10), and downregulated expression of pro-inflammatory cytokines (IL-iβ) (Yang et al., 2017). Future studies should assess pro- and anti-inflammatory cytokine expression profiles in serum and spleen from the hUTC and vehicle treated monkeys to test this hypothesis.

Within days of injection, hUTC migrate to the brain targeting the perilesional area (Arbab et al., 2012), but very few human cells are found in the ischemic cortex 60 days after stroke (Shehadah et al., 2013; Zhang et al., 2013, 2012, 2011). *In vitro*, cell based therapies secrete signals that polarize microglia to an alternatively activated phenotype (Fumagalli et al., 2015) and growth factors that encourage dendritic remodeling and synaptogenesis (Alder et al., 2012). *In vivo* studies report that cell based therapies lead to reduction of apoptotic cells (Zhang et al., 2012, 2011), necrotic cells (Shams Ara et al., 2015), and oxidative stress (Calio et al., 2014; Chen et al., 2016) as well as higher vascular and synaptic density in the ischemic boundary zone (Arbab et al., 2012; Jiang et al., 2012; Shehadah et al., 2013; Yang et al., 2012; Zhang et al., 2013, 2012, 2011). Beyond the lesion area, small changes in remyelination and reorganization are plausible mechanisms underlying restored function with cell therapy treatment. Previously, we reported an increased activation of c-Fos in neurons of ventral premotor cortices as a mechanism of reorganization with hUTC that was related to improved recovery (Orczykowski et al., 2018) confirming other published results (Frost et al., 2003; Nudo, 2007; Nudo and McNeal, 2013). The current study suggests that systemic hUTC infusion may be associated with a higher recruitment of microglia and a reduction of secondary damage. These changes may have led to more effective reorganization and remyelination, which we observed as improved motor function after injury.

3.8 Conclusion

In this study, we provided for the first time a report of the histopathology observed in a non-human primate model of cortical injury treated with a systemic cell based therapy containing hUTC. The major findings of this study are the reduction of oxidative damage and iron accumulation as well as increased extent of activation of microglia observed with the administration of a cell based therapy. These findings provide confirmation of previously published studies and insight into the mechanism of cell based therapies in recovery from stroke.

4. EXPERIMENTAL PROCEDURE

4.1.1 Subjects—Subjects were 8 young adult male rhesus monkeys (*Macaca mulatta*), between 8.5 and 12.1 years old, approximately equivalen t to humans between 24 and 36

based on Tigges et al., (1988). They were all part of a previous study (Moore et al., 2013) to assess the efficacy of human umbilical tissue-derived cell therapy on recovery of motor function following unilateral injury to the hand representation of primary motor cortex. Subject information, including treatment and reconstructed lesion volume are summarized in Table 1. Prior to entering the treatment study, all monkeys received medical examinations and were screened to ensure they did not have a history of malnutrition, diabetes, chronic illness, or any neurological problems. They were given initial pre-operative MRI scans to ensure no occult brain abnormality. While enrolled in the study, monkeys were housed in the Laboratory Animal Science Center of Boston University Medical Campus, which is accredited by the Association for the Assessment and Accreditation of Laboratory Animal Care (AAALAC). Experiments were conducted in accordance with the Guide for the Care and Use of Laboratory Animals from the National Institute of Health's Office of Laboratory Animal Welfare and were approved by the Institutional Animal Care and Use Committee (IACUC) of Boston University Medical Campus. Behavioral testers, surgeons, and other research staff were blind to treatment condition throughout the experiment including tissue processing and data analysis. Behavioral findings demonstrating a positive effect on recovery of motor function and an anatomical examination identifying the intact, ipsilesional ventral premotor cortex as a likely contributor to this recovery have been published (Moore et al., 2013; Orczykowski et al., 2018). Testing and surgical procedures have been detailed in previous studies (Moore et al., 2010, 2013, 2012) and are briefly described below.

4.1.2 Pre-operative Training on Fine Motor Function Tasks—

As previously described (Moore et al., 2010, 2013, 2012) monkeys were pre-trained on our Hand Dexterity Task (HDT), a modified version of a Klüver board (Klüver, 1935), for a total of five weeks with equal trials performed with each hand, each day. At the completion of pre-training, monkeys were given free choice trials with both sides baited and responding with both hands allowed. The lesion was then targeted to the hemisphere controlling the dominant hand to ensure that monkeys would be motivated to use the impaired hand during post-operative testing.

4.1.3 Electrophysiological Mapping and Lesion of the M1 Hand Area—

As previously reported (Moore et al., 2013), all subjects underwent a craniotomy exposing the precentral gyrus of the hemisphere contralateral to the preferred hand. Then, a small monopolar silver ball electrode was placed gently on the pia and electrical stimulation applied to identify loci from which motor movement of the hand, fingers, thumb or wrist could be evoked at the lowest threshold. A map was created by moving the electrode systematically in rows from the dorsal to the ventral aspect of the pre-central gyrus and marking positive loci onto a calibrated photograph of the gyrus. Using this map, a lesion limited to this identified hand representation was created by making a small incision in the pia at the dorsal limit of the hand representation area and then inserting a small glass suction pipette under the pia to bluntly dissect the small penetrating arterioles as they enter the underlying cortex throughout the region. This approach removes the blood supply to the cortex of the mapped hand representation but does not directly damage cortical gray matter or white matter. This produces an ischemic lesion of the gray matter with preservation of underlying white matter (Moore et al., 2013).

4.1.4 Human Umbilical Tissue Derived Cell Therapy Infusion—Human umbilical tissue-derived cell therapy (hUTC) in a proprietary thaw and inject formulation called CSCV4 (CNTO0007) was supplied by Advanced Technologies and Regenerative Medicine, LLC. Between 23 and 24 hours following surgery hUTC was administered intravenously at a dose of 10 million cells/kg at a concentration of 10 million cells/mL and a rate of 0.5 mL per minute using a syringe pump as described previously (Moore et al., 2013). Placebo monkeys received vehicle administered at the same volume and rate.

4.1.5 Post-operative Testing—Post-operative testing began 14 days after surgery and continued for 12 weeks. To ensure that each monkey used the impaired hand, 70% of the trials required the use of the impaired hand (contralateral to the lesion) while 30% were given to the unaffected hand. Performance during pre-operative and post-operative testing was videotaped from fixed cameras located above each hand testing location. A licensed Occupational Therapist (M.A.P.) who specializes in upper extremity recovery following stroke, analyzed the videotapes using our Grasp Assessment Scale for non-human primates (NHP) (Moore et al., 2012), adapted from scales used in human stroke patients (Carr et al., 1985; Fugl-Meyer et al., 1975; Whishaw et al., 2002). Our NHP scale ranges from 0 for no movement to 8 for normal grasp with accurate pinch between thumb and finger. A value between 0–8 was assigned to their performance each post-operative testing day and the mean score across the entire post-operative period determined (Moore et al., 2013).

4.1.6 Perfusion and Tissue Acquisition—At the conclusion of the experiment, monkeys were given a final 1 hour testing session with all trials to the impaired hand and 1 hour later were sedated with ketamine (10 mg/kg IM) deeply anesthetized with sodium pentobarbital (25 mg/kg IV to effect). They were then euthanized by exsanguination during transcardia | perfusion-fixation of the brain, first with cold Krebs-Heinsleit buffer (4°C, pH 7.4) and subsequently with 4% paraformaldehyde, (30°C, pH 7.4). The brain was blocked, *in situ*, in the coronal plane to ensure reproducible planes of section during later processing and then removed from the skull, weighed and post-fixed overnight in 4% paraformaldehyde (no more than 18 hours). It was then transferred to cryoprotectant solution to eliminate freezing artifact (Rosene et al., 1986). Cryoprotected blocks were flash frozen at −75°C and stored at −80°C until they were cut on a microtome into interrupted series of coronal sections (eight series of 30 μm thick sections and one series of 60 pm thick sections) with a spacing between sections within a series of 300 pm. The 60 pm series was immediately mounted on microscope slides and stained with thionin for lesion reconstruction (Moore et al., 2013). The other series were collected in phosphate buffer with 15% glycerol and stored at −80°C for later histochemical processing (Estrada et al., 2017).

4.2 Immunohistochemistry

Markers chosen for immunohistochemistry were LN3 antibody, to identify MHC II expressing microglia and macrophages, and 4-hydroxynonenal (4-HNE) antibody, to identify this byproduct of lipid peroxidation. Partial series of 30 μm sections spaced 1200 μm (LN3) or 2400 pm (4-HNE) apart containing the motor cortex in both hemispheres were removed from storage and thawed to room temperature for immunohistochemistry. All the sections from all subjects were batch-processed for each marker (see Estrada et al., 2017 for

discussion of batch processing) in the same reagents at the same time, according to the following steps. First, sections were rinsed in 0.05M Tris-buffered saline (TBS) to remove the glycerol. To increase antigenicity of 4-HNE, tissue sections were first incubated in 9.1 mM citrate buffer at 500 Watts at 40°C for 5 minutes then at room temperature for 30 minutes. To quench endogenous peroxidases, all sections were incubated for 30 minutes in TBS containing 1% sodium borohydride (4-HNE) or 3% H_2O_2 (LN3) followed by washes in TBS. Sections were then incubated for one hour in a blocking solution of 10% Normal Goat Serum (NGS) and 0.4% Triton-X in TBS. The sections were incubated for 48 hours at 4°C with gentle agitation in monoclonal primary antibodies to 4-HNE (anti-4HNE in mouse; 1:500, R&D Systems, Minneapolis, MN) and LN3 (anti-LN3 in mouse; 1:1000, MP Biomedicals, Santa Ana, CA) in a solution containing 2% NGS and 0.1% Triton-X in TBS. The sections were incubated for 48 hours at 4°C with gentle agitation in monoclonal primary antibodies to 4-HNE (anti-4HNE in mouse; 1:500, R&D Systems, Minneapolis, MN, catalog #MAB3249) and LN3 (anti-LN3 in mouse; 1:1000, MP Biomedicals, Santa Ana, CA, catalog #08A003115) in a solution containing 2% NGS and 0.1% Triton-X in TBS. Several sections of brain tissue were left out of the primary antibody to control for immunoreactivity.

Following incubation with the primary antibody, the sections were washed in a solution containing 2% NGS and 0.1% Triton-X in TBS, followed by a 2-hour incubation in biotinylated secondary antibody (1:600; Vector Laboratories, Burlingame, CA) in TBS containing 2% NGS, and 0.4% Triton-X. The sections were then washed in TBS and subsequently incubated with an avidin biotinylated horseradish peroxidase complex (ABC Elite; Vector Laboratories, Burlingame, CA) for 1 hour. The sections were then washed in TBS followed by rinses in 0.175M sodium acetate solution. For visualization, all sections were incubated together in sodium acetate containing 0.55mM 3–3'-diaminobenzidine (DAB; Sigma-Aldrich, St. Louis, MO), nickel sulfate (0.095M), and 0.0025% H_2O_2. The sections were washed in sodium acetate to stop the DAB reaction, followed by rinses in TBS. Finally, sections were mounted on gelatin-coated slides, air dried, and cover-slipped using Permount mounting medium (Thermo Fisher Scientific, Waltham, MA).

Sections stained with the antibody to LN3 were counterstained with 0.5% thionin (Fisher Scientific, Pittsburgh, PA) to define the boundary between the gray and white matter. Briefly, slides containing LN3 stained sections were rehydrated through a graded series of ethanol to water and then incubated for 2 minutes in filtered 0.5% thionin solution (pH 5.5) containing sodium acetate and glacial acetic acid. After rinsing, slides were dehydrated through a graded series of ethanol (70%, 95%, 100%, 100%), cleared in Xylene (Fisher Scientific, Pittsburgh, PA) and coverslipped using Permount mounting medium (Thermo Fisher Scientific, Waltham, MA).

4.3 Iron Histology

A series of 30 μm sections spaced at 1200 pm and containing the motor cortex in both hemispheres was removed from storage and mounted on gelatin subbed microscope slides and allowed to dry completely. For Perl's Prussian Blue stain, slides were immersed in dH_2O for one minute. Next, a solution of 5% Hydrochloric Acid (HCl; Fisher Scientific,

Pittsburgh, PA) and 5% Potassium Ferrocyanide (Sigma-Aldrich, St. Louis, MO) in dH_2O (Prussian Blue Solution) was prepared immediately before use and slides incubated for 35 minutes. Following this, slides were moved through two rounds of dH_2O and dehydrated through a graded series of ethanol (70%, 95%, 100%, 100%). Finally, slides were cleared in Xylene (Fisher Scientific, Pittsburgh, PA) and coverslipped using Permount (Thermo Fisher Scientific, Waltham, MA).

4.4 Regions of Interest for Stereology and Densitometry

Data collection was done with the experimenter blind to the treatment condition of each monkey. Regions of interest (ROI) for 4-HNE densitometry and LN3 stereology were determined with the 4× objective on a Nikon E600 light microscope and included perilesional gray matter (PLG) and sublesional white matter (SLW) (Figure 9B). The SLW ROI was defined by drawing a straight line from the depths of the cingulate sulcus (1) to the depths of the circular sulcus (2) on the dorsal aspect of the insula. Next, a line perpendicular to the cortical surface was drawn from the circular sulcus (2) to the gray-white boundary (3). The next line followed the gray white boundary to a point in line with the cingulate sulcus (1). Finally, a line perpendicular to the cortical surface was drawn to connect the medial aspect of the gray-white boundary (4) with the cingulate sulcus (1). The PLG ROI was defined starting at the medial aspect of the gray-white boundary (4) and following the gray-white boundary to the lateral aspect (3). Next, a parallel line to SLW 2–3 was drawn from 3 to the cortical surface (5). The next line followed the cortical surface to a point (6) in line with the cingulate sulcus (1). Finally, a line was drawn to connect the cortical surface (6) to the gray-white boundary (4). The ROI for iron histology (affected cortex) was defined as the presence of strong Prussian Blue staining around the lesion to its medial and lateral boundaries and as deep into the white matter as the strong staining extended (Figure 9C). The reconstructed lesion volume represents cortex lost and the volume of affected cortex represents the extent cortex with iron accumulation and gliosis.

4.5 Densitometry for 4-HNE

The percent area of staining was quantified for 4-HNE. Mounted sections stained for 4-HNE were visualized on a Nikon E600 light microscope equipped with a motorized stage and Surveyor software with TurboScan (Objective Imaging, Kansasville, WI). Two sections spaced 2400 μm within 5 mm of the lesion site were selected for analysis. The ipsilesional hemisphere was visualized in Surveyor using the 4× objective, bright field correction, and manual focus. Brightness and exposure were kept constant for all sections from all subjects. Tiled images including both the PLG and SLW ROIs were acquired and saved as TIFF files. These images were imported into Fiji software (NIH, version 1.50i), (Schindelin et al., 2012) and scale was set using distance in pixels of 1.59245 μm/pixel. ROIs (PLG and SLW) were traced and saved in the ROI Manager (Figure 9B). Image ROIs were transformed into 8-bit images and the threshold function (percentile) was used to create binary images and remove artifact. Measurements were set to calculate “Area Fraction” and these measurements were saved for analysis. The density of 4-HNE label as a measure of oxidative stress is reported as a percentage of staining following threshold within the ROI defined.

4.6 Densitometry for Iron Histology

Mounted sections stained with Prussian Blue were visualized on a Nikon E600 light microscope equipped with a motorized stage and Nikon Imaging Software (NIS - Advanced Research). Sections spaced every 1200 μm throughout 7 to 10 mm of the lesion site were selected for analysis which was 6–8 sections selected per animal. The investigator was blind to the subject descriptions and experimental conditions. Tiled Images of the area of iron accumulation (affected cortex) (Figure 9C) were acquired using the 10× objective. All images were acquired using 750 psec exposure and AutoWhite balance. Focus was determined using “Focus Surface” wherein the surface of the tissue on which to focus was interpolated using 5 manually focused reference points per tissue section. The tiled images were overlapped by 10% as collected and then stitched via blending and image registration. Once acquired, images as nd2 (proprietary Nikon format) files were analyzed using the Nikon NIS-AR analysis software polygon tool to outline the full extent of Prussian Blue staining in the lesion area. Then, RGB Threshold was determined by 3- or 6-point threshold tool limited to the defined area. ROI Statistics were exported to Excel and numbers used include “ROI Area,” “Area Fraction,” and “ROI Mean Intensity.” Mean Intensity measures (optical density) were inverted by subtracting numbers from 4095 (maximum for RGB intensity) such that the larger numbers represent a darker intensity of staining and the lower numbers represent a lighter intensity of staining. The total volume of iron accumulation was then determined using the Cavalieri estimator (Rosen and Harry, 1990) by taking the sum of the outlined ROI areas of each section and multiplying by the distance (1.2 mm) between sections to estimate volume.

4.7 LN3 Stereology

Unbiased stereology was used to quantify LN3 labeled microglia visualized on a Nikon Eclipse E600 series light microscope (Nikon; Melville, NY, USA) equipped with a motorized stage integrated with StereoInvestigator 9 software (MicroBrightField Bioscience; Williston, VT). The Optical Fractionator Workflow on StereoInvestigator was used to quantify 6–8 sections spaced every 1200 μm throughout 7 to 10 mm of the lesion site in motor cortex. ROI (PLG and SLW) were determined at 4× objective. The Optical Fractionator Workflow places a sampling grid over the ROI using systematic random sampling. The sampling grid was optimized at 1000μm × 1000μm for the PLG and 1300 pm × 1300 pm for the SLW. However, to gain sufficient correlation of error for stereology (Gundersen et al., 1999), the subcortica ｜ white matter was recounted in 3 animals (2 control and 1 treated) using a sampling grid of 800 μm × 800 μm.

Cells were counted within a three-dimensional counting frame placed at a fixed corner of each sampling grid square. Sections were visualized at 20× objective with a counting frame of 475 μm × 275 μm. The height of this box was 15 μm. To ensure unbiased counting, 2 μm guard zones above and below the box were used to ensure that lost caps could be identified and counted or excluded according to the respective face (West et al., 1991). Inclusion criteria included a well-defined cell body located within the counting frame. Markers used for stereology categorized each microglia counted as either ramified, hypertrophic, or amoeboid using a previously published study as a guide (Karperien et al., 2013) as a guide. The estimated total number of LN3 positive microglia by phenotype in each ROI were

calculated using the optical fractionator formula (Sutula and West, 2002; West et al., 1991). Parameters were optimized such that Coefficients of Error were less than 0.10 using a Smoothness Factor m=1 for biological tissue (Gundersen et al., 1999). The density measures of each phenotype were reported in order to account for variability in the volume of traced regions of interest between subjects. The density of microglia per mm^3 was calculated by dividing the "estimated population using number weighted section thickness" by the volume calculated by Cavalieri estimator in StereoInvestigator.

4.8 LN3 Total Area Stained

LN3+ cells extended beyond the perilesional and sublesional areas and differed between individuals. In order to quantify these differences, mounted sections were digitized on a Nikon E600 light microscope equipped with a motorized stage using Nikon Imaging Software (NIS - Advanced Research). Tiled whole hemisphere images were acquired with the 1× objective from 6–8 sections containing primary motor cortex, and white matter of the corpus callosum, frontal white matter, internal capsule, cerebral peduncle, and temporal lobe white matter. Ratings between 0 and 4 were given to each of the regions specified above in both ipsilesional and contralesional hemispheres with the investigator blind to treatment conditions. A rating of 0 indicated no staining present. A rating of 1 indicated a baseline staining present; 2 indicated medium staining; 3 indicated strong staining; and 4 indicated intense staining. These ratings were separated by region and by hemisphere (ipsilesional and contralesional). One outline was made around all regions with a rating of 2, 3, or 4 to calculate a total area (μm^2) stained. Numbers used for comparison between treatment groups included total gray matter area stained, total white matter area stained, and region ratings.

4.9 Data Analysis and Statistics

The data were analyzed using R (RStudio Inc, Version 0.99.896, R foundation for Statistical Computing, Vienna, Austria). A student's one-tailed t test ($\alpha = 0.05$) was used to evaluate group differences for 1) area fraction of oxidative damage, 2) iron accumulation volume of affected cortex, percent area stained, and optical density for Prussian Blue histology, and 3) area stained of LN3. Bonferroni correction was used to adjust p value threshold for multiple comparisons. Kruskal Wallis H test was used to compare regional microglial ratings as an ordinal scale. For microglia stereology, two-way ANOVA with repeated measures was used to identify significant variables and interactions with group (vehicle or hUTC treated) as a between subject variable and cell type (ramified, hypertrophic, and amoeboid) as within subject variables. Correlations were assessed using a Pearson's correlations between oxidative damage in PLG, amoeboid microglia in PLG, iron volume, and reconstructed lesion volume.

ACKNOWLEDGEMENTS

This study was supported by a contract from Advanced Technologies and Regenerative Medicine (ATRM), LLC. [RR# 101115-PR] who provided the cell therapy product and the vehicle control and by the National Institutes of Health [NIH-NINDS R21NS081261]. We thank Megan McBurnie, Melissa Joblin, Reese Edwards, and Karen Slater for their expert technical assistance with all aspects of this study. On December 30, 2012, ATRM merged into DePuy Orthopaedics, Inc.

BIBLIOGRAPHY

Alder J, Kramer BC, Hoskin C, Thakker-Varia S, 2012 Brain-derived neurotrophicfactor produced by human umbilical tissue-derived cells is required for its effect on hippocampal dendritic differentiation. Dev. Neurobiol 72, 755–765. 10.1002/dneu.20980 [PubMed: 21954108]

Amantea D, Micieli G, Tassorelli C, Cuartero MI, Ballesteros I, Certo M, Moro MA, Lizasoain I, Bagetta G, 2015 Rational modulation of the innate immune system for neuroprotection in ischemic stroke. Front. Neurosci 9, 147 10.3389/fnins.2015.00147 [PubMed: 25972779]

Anttila JE, Whitaker KW, Wires ES, Harvey BK, Airavaara M, 2016 Role of microglia in ischemic focal stroke and recovery: Focus on Toll-like receptors. Prog. NeuroPsychopharmacology Biol. Psychiatry 10.1016/j.pnpbp.2016.07.003

Arbab AS, Thiffault C, Navia B, Victor SJ, Hong K, Zhang L, Jiang Q, Varma NR, Iskander A, Chopp M, 2012 Tracking of In-111-labeled human umbilical tissue-derived cells (hUTC) in a rat model of cerebral ischemia using SPECT imaging. BMC Med. Imaging 12, 33 10.1186/1471-2342-12-33 [PubMed: 23217090]

Bresgen N, Eckl P, 2015 Oxidative Stress and the Homeodynamics of Iron Metabolism. Biomolecules 5, 808–847. 10.3390/biom5020808 [PubMed: 25970586]

Brouns R, De Deyn PP, 2009 The complexity of neurobiological processes in acute ischemic stroke. Clin. Neurol. Neurosurg 111, 483–95. 10.1016/j.clineuro.2009.04.001 [PubMed: 19446389]

Calió ML, Marinho DS, Ko GM, Ribeiro RR, Carbonel AF, Oyama LM, Ormanji M, Guirao TP, Calio PL, Reis LA, Simoes MDJ, Lisbôa-Nascimento T, Ferreira AT, Bertoncini CRA, 2014 Transplantation of bone marrow mesenchymal stem cells decreases oxidative stress, apoptosis, and hippocampal damage in brain of a spontaneous stroke model. Free Radic. Biol. Med 70, 141–154. 10.1016/j.freeradbiomed.2014.01.024 [PubMed: 24525001]

Carr JH, Shepherd RB, Nordholm L, Lynne D, 1985 Investigation of a new motor assessment scale for stroke patients. Phys. Ther 65, 175–80. [PubMed: 3969398]

Chen KH, Chen CH, Wallace CG, Yuen CM, Kao GS, Chen YL, Shao PL, Chen YL, Chai HT, Lin KC, Liu CF, Chang HW, Lee MS, Yip HK, 2016 Intravenous administration of xenogenic adipose-derived mesenchymal stem cells (ADMSC) and ADMSC-derived exosomes markedly reduced brain infarct volume and preserved neurological function in rat after acute ischemic stroke. Oncotarget 7 10.18632/oncotarget.12902

Demougeot C, Van Hoecke M, Bertrand N, Prigent-Tessier A, Mossiat C, Beley A, Marie C, 2004 Cytoprotective efficacy and mechanisms of the liposoluble iron chelator 2,2'-dipyridyl in the rat photothrombotic ischemic stroke model. J. Pharmacol. Exp. Ther 311, 1080–7. 10.1124/jpet.104.072744 [PubMed: 15280435]

Estrada LI, Robinson AA, Amaral AC, Giannaris EL, Heyworth NC, Mortazavi F, Ngwenya LB, Roberts DE, Cabral HJ, Killiany RJ, Rosene DL, 2017 Evaluation of Long-Term Cryostorage of Brain Tissue Sections for Quantitative Histochemistry. J. Histochem. Cytochem 002215541668693. 10.1369/0022155416686934

Eyo UB, Dailey ME, 2013 Microglia: Key elements in neural development, plasticity, and pathology. J. Neuroimmune Pharmacol 8, 494–509. 10.1007/s11481-013-9434-z [PubMed: 23354784]

Frost SB, Barbay S, Friel KM, Plautz EJ, Nudo RJ, 2003 Reorganization of remote cortical regions after ischemic brain injury: a potential substrate for stroke recovery. J. Neurophysiol 89, 3205–14. 10.1152/jn.01143.2002 [PubMed: 12783955]

Fugl-Meyer A, Jaasko L, Leyman I, Olsson S, Steglind S, 1975 The post-stroke hemiplegic patient. Scand J Rehabil Med 7, 13–31. [PubMed: 1135616]

Fumagalli S, Perego C, Pischiutta F, Zanier ER, De Simoni M-G, 2015 The ischemic environment drives microglia and macrophage function. Front. Neurol 6, 81 10.3389/fneur.2015.00081 [PubMed: 25904895]

Gundersen H, Jensen E, Kieu K, Nielsen J, 1999 The efficiency of systematic sampling in stereology —reconsidered. J. Microsc 193, 199–211. [PubMed: 10348656]

Gutteridge JM, Hou YY, 1986 Iron complexes and their reactivity in the bleomycin assay for radical-promoting loosely-bound iron. Free Radic. Res. Commun 2, 143–51. [PubMed: 2463216]

Gutteridge JMC, 2006 Hydroxyl Radicals, Iron, Oxidative Stress, and Neurodegenerationa. Ann. N. Y. Acad. Sci 738, 201–213. 10.1111/j.1749-6632.1994.tb21805.x

Jiang Q, Thiffault C, Kramer BC, Ding GL, Zhang L, Nejad-Davarani SP, Li L, Arbab AS, Lu M, Navia B, Victor SJ, Hong K, Li QJ, Wang SY, Li Y, Chopp M, 2012 MRI detects brain reorganization after human umbilical tissue-derived cells (hUTC) treatment of stroke in rat. PLoS One 7, 1–11. 10.1371/journal.pone.0042845

Jiang X, Pu H, Hu X, Wei Z, Hong D, Zhang W, Gao Y, Chen J, Shi Y, 2016 A Post-stroke Therapeutic Regimen with Omega-3 Polyunsaturated Fatty Acids that Promotes White Matter Integrity and Beneficial Microglial Responses after Cerebral Ischemia. Transl. Stroke Res 7, 548–561. 10.1007/s12975-016-0502-6 [PubMed: 27714669]

Karperien A, Ahammer H, Jelinek HF, 2013 Quantitating the subtleties of microglial morphology with fractal analysis. Front. Cell. Neurosci 7, 3 10.3389/fncel.2013.00003 [PubMed: 23386810]

Klüver H, 1935 An Auto-Multi-Stimulation Reaction Board for Use with Sub-Human Primates. J. Psychol 1, 123–127.

Koh S, Chen WJ, Dejneka NS, Harris IR, Lu B, Girman S, Saylor J, Wang S, Eroglu C, 2018 Subretinal Human Umbilical Tissue-Derived Cell Transplantation Preserves Retinal Synaptic Connectivity and Attenuates Müller Glial Reactivity. J. Neurosci 38, 1532–17. 10.1523/JNEUROSCI.1532-17.2018

Koh S, Kim N, Yin HH, Harris IR, Dejneka NS, Eroglu C, 2015 Human Umbilical Tissue-Derived Cells Promote Synapse Formation and Neurite Outgrowth via Thrombospondin Family Proteins. J. Neurosci 35, 15649–65. 10.1523/JNEUROSCI.1364-15.2015 [PubMed: 26609158]

Kreutzberg GW, 1996 Microglia: A sensor for pathological events in the CNS. Trends Neurosci 19, 312–318. 10.1016/0166-2236(96)10049-7 [PubMed: 8843599]

Lalancette-Hebert M, Gowing G, Simard A, Weng YC, Kriz J, 2007 Selective ablation of proliferating microglial cells exacerbates ischemic injury in the brain. J. Neurosci 27, 2596–2605. 10.1523/JNEUROSCI.5360-06.2007 [PubMed: 17344397]

Lampron A, Larochelle A, Laflamme N, Prefontaine P, Plante M-M, Sanchez MG, Yong VW, Stys PK, Tremblay M-E, Rivest S, 2015 Inefficient clearance of myelin debris by microglia impairs remyelinating processes. J. Exp. Med 212, 481–495. 10.1084/jem.20141656 [PubMed: 25779633]

Liguz-Lecznar M, Kossut M, 2013 Influence of inflammation on poststroke plasticity. Neural Plast 2013, 258582 10.1155/2013/258582 [PubMed: 23533818]

Lipton P, 1999 Ischemic cell death in brain neurons. Physiol. Rev 79, 1431–1568. 10.1016/j.shpsa.2008.02.001 [PubMed: 10508238]

London A, Cohen M, Schwartz M, 2013 Microglia and monocyte-derived macrophages: functionally distinct populations that act in concert in CNS plasticity and repair. Front. Cell. Neurosci 7, 34 10.3389/fncel.2013.00034 [PubMed: 23596391]

Mimica-Duki N, Simin N, Svirev E, Ori D, Beara I, Lesjak M, Boi B, 2012 The Effect of Plant Secondary Metabolites on Lipid Peroxidation and Eicosanoid Pathway, in: Lipid Peroxidation InTech 10.5772/48193

Minotti G, Aust SD, 1989 The role of iron in oxygen radical mediated lipid peroxidation. Chem. Biol. Interact 71, 1–19. [PubMed: 2550151]

Moore T, Killiany R, Pessina M, Moss M, Rosene D, 2010 Assessment of motor function of the hand in aged rhesus monkeys. Somatosens. Mot. Res 27, 121–130. [PubMed: 20653499]

Moore TL, Killiany RJ, Pessina MA, Moss MB, Finklestein SP, Rosene DL, 2012 Recovery from ischemia in the middle-aged brain: A nonhuman primate model. Neurobiol. Aging 33, 619.e9–619.e24. 10.1016/j.neurobiolaging.2011.02.005

Moore TL, Pessina MA, Finklestein SP, Kramer BC, Killiany RJ, Rosene DL, 2013 Recovery of fine motor performance after ischemic damage to motor cortex is facilitated by cell therapy in the rhesus monkey. Somatosens. Mot. Res 30, 185–96. 10.3109/08990220.2013.790806 [PubMed: 23758412]

Narantuya D, Nagai A, Abdullah M, Masuda J, Kobayashi S, Yamaguchi S, Kim SU, 2010 Human microglia transplanted in rat focal ischemia brain induce neuroprotection and behavioral improvement. PLoS One 5 10.1371/journal.pone.0011746

Navarro-Yepes J, Zavala-Flores L, Anandhan A, Wang F, Skotak M, Chandra N, Li M, Pappa A, Martinez-Fong D, Del Razo LM, Quintanilla-Vega B, Franco R, 2014 Antioxidant gene therapy against neuronal cell death. Pharmacol. Ther 142, 206–230. 10.1016/j.pharmthera.2013.12.007 [PubMed: 24333264]

Nudo RJ, 2007 Postinfarct cortical plasticity and behavioral recovery. Stroke 38, 840–845. 10.1161/01.STR.0000247943.12887.d2 [PubMed: 17261749]

Nudo RJ, McNeal D, 2013 Plasticity of cerebral functions. Handb. Clin. Neurol 110, 13–21. 10.1016/B978-0-444-52901-5.00002-2 [PubMed: 23312627]

Ohtaki H, Ylostalo JH, Foraker JE, Robinson AP, Reger RL, Shioda S, Prockop DJ, 2008 Stem/progenitor cells from bone marrow decrease neuronal death in global ischemia by modulation of inflammatory/immune responses. Proc. Natl. Acad. Sci 105, 14638–14643. 10.1016/S0140-6736(17)30761-4 [PubMed: 18794523]

Orczykowski ME, Arndt KR, Palitz LE, Kramer BC, Pessina MA, Oblak AL, Finklestein SP, Mortazavi F, Rosene DL, Moore TL, 2018 Cell based therapy enhances activation of ventral premotor cortex to improve recovery following primary motor cortex injury. Exp. Neurol 305, 13–25. 10.1016/j.expneurol.2018.03.010 [PubMed: 29540323]

Patel AR, Ritzel R, McCullough LD, Liu F, 2013 Microglia and ischemic stroke: A double-edged sword. Int. J. Physiol. Pathophysiol. Pharmacol 5, 73–90. [PubMed: 23750306]

Perego C, Fumagalli S, De Simoni M-G, Davalos D, Grutzendler J, Yang G, Kim J, Zuo Y, Jung S, Littman D, Dustin M, Gan W, Yenari M, Kauppinen T, Swanson R, Iadecola C, Anrather J, Jin R, Yang G, Li G, Schilling M, Besselmann M, Muller M, Strecker J, Ringelstein E, Kiefer R, Block M, Zecca L, Hong J, Hanisch U, Capone C, Frigerio S, Fumagalli S, Gelati M, Principato M, Storini C, Montinaro M, Kraftsik R, De Curtis M, Parati E, De Simoni M, Lalancette-Hebert M, Gowing G, Simard A, Weng Y, Kriz J, Neumann J, Gunzer M, Gutzeit H, Ullrich O, Reymann K, Dinkel K, Nakajima K, Yamamoto S, Kohsaka S, Kurihara T, Stoll G, Jander S, Thored P, Heldmann U, Gomes-Leal W, Gisler R, Darsalia V, Taneera J, Nygren J, Jacobsen S, Ekdahl C, Kokaia Z, Lindvall O, Lu Y, Lin C, Cheng F, Hsueh C, Batchelor P, Liberatore G, Wong J, Porritt M, Frerichs F, Donnan G, Howells D, David S, Kroner A, Porta C, Rimoldi M, Raes G, Brys L, Ghezzi P, Di Liberto D, Dieli F, Ghisletti S, Natoli G, De Baetselier P, Michelucci A, Heurtaux T, Grandbarbe L, Morga E, Heuschling P, Penninger J, Irie-Sasaki J, Sasaki T, Oliveira-dos-Santos A, Bhatia S, Fei M, Yarlagadda M, Qi Z, Akira S, Saijo S, Iwakura Y, van Rooijen N, Gibson G, Croix CS, Raes G, Noel W, Beschin A, Brys L, de Baetselier P, Hassanzadeh G, Gesuete R, Storini C, Fantin A, Stravalaci M, Zanier E, Orsini F, Vietsch H, Mannesse M, Ziere B, Gobbi M, De Simoni M, Storini C, Bergamaschini L, Gesuete R, Rossi E, Maiocchi D, De Simoni M, De Simoni M, Storini C, Barba M, Catapano L, Arabia A, Rossi E, Bergamaschini L, Swanson R, Morton M, Tsao-Wu G, Savalos R, Davidson C, Sharp F, Donnelly D, Gensel J, Ankeny D, Rooijen N. van, Popovich P, Ortolano F, Colombo A, Zanier E, Sclip A, Longhi L, Perego C, Stocchetti N, Borsello T, De Simoni M, Longhi L, Gesuete R, Perego C, Ortolano F, Sacchi N, Villa P, Stocchetti N, De Simoni M, Santosh C, Brennan D, McCabe C, Macrae I, Holmes W, Graham D, Gallagher L, Condon B, Hadley D, Muir K, Gsell W, Faul F, Erdfelder E, Lang A, Buchner A, Sedgwick J, Schwender S, Imrich H, Dorries R, Butcher G, ter Meulen V, Stein V, Baumgartner W, Schroder S, Zurbriggen A, Vandevelde M, Tipold A, Colton C, Lambertsen K, Clausen B, Babcock A, Gregersen R, Fenger C, Nielsen H, Haugaard L, Wirenfeldt M, Nielsen M, Dagnaes-Hansen F, Reed-Geaghan E, Reed Q, Cramer P, Landreth G, Shin J, Lee J, Lee J, Min W, Schuchman E, Jin H, Bae J, Ohtaki H, Ylostalo J, Foraker J, Robinson A, Reger R, Shioda S, Prockop D, Ponomarev E, Maresz K, Tan Y, Dittel B, Kigerl K, Gensel J, Ankeny D, Alexander J, Donnelly D, Popovich P, Solovjov D, Pluskota E, Plow E, Gelderblom M, Leypoldt F, Steinbach K, Behrens D, Choe C, Siler D, Arumugam T, Orthey E, Gerloff C, Tolosa E, Magnus T, Ajami B, Bennett J, Krieger C, McNagny K, Rossi F, de Beer M, Zhao Z, Webb N, Westhuyzen D. van der, de Villiers W, Ramprasad M, Terpstra V, Kondratenko N, Quehenberger O, Steinberg D, Jayadev S, Nesser N, Hopkins S, Myers S, Case A, Lee R, Seaburg L, Uo T, Murphy S, Morrison R, Garden G, Denes A, Vidyasagar R, Feng J, Narvainen J, McColl B, Kauppinen R, Allan S, Zanier E, Montinaro M, Vigano M, Villa P, Fumagalli S, Pischiutta F, Longhi L, Leoni M, Rebulla P, Stocchetti N, Chang L, Karin M, Porcheray F, Viaud S, Rimaniol A, Leone C, Samah B, Dereuddre-Bosquet N, Dormont D, Gras G, Linehan J, Kolios G, Valatas V, Robertson D, Westwick J, Kettenmann H, 2011 Temporal pattern of expression and colocalization of microglia/

macrophage phenotype markers following brain ischemic injury in mice. J. Neuroinflammation 8, 174 10.1186/1742-2094-8-174 [PubMed: 22152337]

Rana AK, Singh D, 2018 Targeting glycogen synthase kinase-3 for oxidative stress and neuroinflammation: Opportunities, challenges and future directions for cerebral stroke management. Neuropharmacology 139, 124–136. 10.1016/j.neuropharm.2018.07.006 [PubMed: 30017999]

Ravera S, Bartolucci M, Cuccarolo P, Litame E, Illarcio M, Calzia D, Degan P, Morelli A, Panfoli I, 2015 Oxidative stress in myelin sheath: The other face of the extramitochondrial oxidative phosphorylation ability. Free Radic. Res 49, 1–36. 10.3109/10715762.2015.1050962 [PubMed: 25241851]

Rosen GD, Harry JD, 1990 Brain volume estimation from serial section measurements: a comparison of methodologies. J. Neurosci. Methods 35, 115–24. [PubMed: 2283883]

Rosene DL, Roy NJ, Davis BJ, 1986 A cryoprotection method that facilitates cutting frozen sections of whole monkey brains for histological and histochemical processing without freezing artifact. J. Histochem. Cytochem 34, 1301–1315. 10.1177/34.10.3745909 [PubMed: 3745909]

Satani N, Savitz SI, 2016 Is Immunomodulation a Principal Mechanism Underlying How Cell-Based Therapies Enhance Stroke Recovery? Neurotherapeutics 13, 775–782. 10.1007/s13311-016-0468-9 [PubMed: 27485235]

Savitz SI, Cramer SC, Wechsler L, STEPS 3 Consortium, 2014 Stem cells as an emerging paradigm in stroke 3: enhancing the development of clinical trials. Stroke 45, 634–9. 10.1161/STROKEAHA.113.003379 [PubMed: 24368562]

Schindelin J, Arganda-Carreras I, Frise E, Kaynig V, Longair M, Pietzsch T, Preibisch S, Rueden C, Saalfeld S, Schmid B, Tinevez J, White DJ, Hartenstein V, Eliceiri K, Tomancak P, Cardona A, 2012 Fiji: an open-source platform for biological-image analysis. Nat. Methods 9, 676–682. 10.1038/nmeth.2019 [PubMed: 22743772]

Selim MH, Ratan RR, 2004 The role of iron neurotoxicity in ischemic stroke. Ageing Res. Rev 3, 345–353. 10.1016/j.arr.2004.04.001 [PubMed: 15231241]

Shams Ara A, Sheibani V, Esmaeilpour K, Eslaminejad T, Nematollahi-Mahani SN, 2015 Coadministration of the Human Umbilical Cord Matrix-Derived Mesenchymal Cells and Aspirin Alters Postischemic Brain Injury in Rats. J. Stroke Cerebrovasc. Dis 24, 2005–2016. 10.1016/j.jstrokecerebrovasdis.2015.04.049 [PubMed: 26145764]

Shehadah A, Chen J, Kramer B, Zacharek A, Cui Y, Roberts C, Lu M, Chopp M, 2013 Efficacy of Single and Multiple Injections of Human Umbilical Tissue-Derived Cells following Experimental Stroke in Rats. PLoS One 8 10.1371/journal.pone.0054083

Shichita T, Ito M, Yoshimura A, 2014 Post-ischemic inflammation regulates neural damage and protection. Front. Cell. Neurosci 8, 319 10.3389/fncel.2014.00319 [PubMed: 25352781]

Shobin E, Bowley MP, Estrada LI, Heyworth NC, Orczykowski ME, Eldridge SA, Calderazzo SM, Mortazavi F, Moore TL, Rosene DL, 2017 Microglia activation and phagocytosis: relationship with aging and cognitive impairment in the rhesus monkey. GeroScience 39, 199–220. 10.1007/s11357-017-9965-y [PubMed: 28238188]

Sutula T, West MJ, 2002 Design-based stereological methods for counting neurons. Prog. Brain Res 135, 43–51. 10.1016/S0079-6123(02)35006-4 [PubMed: 12143362]

Tigges J, Gordon T, McClure H, Hall E, Peters A, 1988 Survival rate and life span of rhesus monkeys at the Yerkes Regional Primate Research Center. Am. J. Primatol 15, 263–273.

West MJ, Slomianka L, Gundersen HJG, 1991 Unbiased stereological estimation of the total number of neurons in the subdivisions of the rat hippocampus using the optical fractionator. Anat. Rec 231, 482–497. 10.1002/ar.1092310411 [PubMed: 1793176]

Whishaw IQ, Suchowersky O, Davis L, Sarna J, Metz GA, Pellis SM, 2002 Impairment of pronation, supination, and body co-ordination in reach-to-grasp tasks in human Parkinson's disease (PD) reveals homology to deficits in animal models. Behav. Brain Res 133, 165–176. 10.1016/S0166-4328(01)00479-X [PubMed: 12110450]

Winterbourn CC, 1995 Toxicity of iron and hydrogen peroxide: the Fenton reaction. Toxicol. Lett 82–83, 969–974. 10.1016/0378-4274(95)03532-X

Yang B, Hamilton JA, Valenzuela KS, Bogaerts A, Xi XP, Aronowski J, Mays RW, Savitz SI, 2017 Multipotent Adult Progenitor Cells Enhance Recovery After Stroke by Modulating the Immune Response from the Spleen. Stem Cells 35, 1290–1302. 10.1002/stem.2600 [PubMed: 28263009]

Yang D, Han Y, Zhang J, Seyda A, Chopp M, Seyfried DM, 2012 Therapeutic effect of human umbilical tissue-derived cell treatment in Rats with experimental intracerebral hemorrhage. Brain Res 1444, 1–10. 10.1016/j.brainres.2012.01.024 [PubMed: 22341873]

Yoo SW, Chang DY, Lee HS, Kim GH, Park JS, Ryu BY, Joe EH, Lee YD, Kim SS, Suh-Kim H, 2013 Immune following suppression mesenchymal stem cell transplantation in the ischemic brain is mediated by TGF-p. Neurobiol. Dis 58, 249–257. 10.1016/j.nbd.2013.06.001 [PubMed: 23759293]

Yoon J-K, Park B-N, Shim W-Y, Shin JY, Lee G, Ahn YH, 2010 In vivo tracking of 1111n-labeled bone marrow mesenchymal stem cells in acute brain trauma model. Nucl. Med. Biol 37, 381–388. 10.1016/j.nucmedbio.2009.12.001 [PubMed: 20346878]

Zanier ER, Montinaro M, Vigano M, Villa P, Fumagalli S, Pischiutta F, Longhi L, Leoni ML, Rebulla P, Stocchetti N, Lazzari L, De Simoni M-G, 2011 Human umbilical cord blood mesenchymal stem cells protect mice brain after trauma. Crit. Care Med 39, 2501–10. 10.1097/CCM.0b013e31822629ba [PubMed: 21725237]

Zanier ER, Pischiutta F, Riganti L, Marchesi F, Turola E, Fumagalli S, Perego C, Parotto E, Vinci P, Veglianese P, D'Amico G, Verderio C, De Simoni MG, 2014 Bone Marrow Mesenchymal Stromal Cells Drive Protective M2 Microglia Polarization After Brain Trauma. Neurotherapeutics 11, 679–695. 10.1007/s13311-014-0277-y [PubMed: 24965140]

Zhang L, Li Y, Romanko M, Kramer BC, Gosiewska A, Chopp M, Hong K, 2012 Different routes of administration of human umbilical tissue-derived cells improve functional recovery in the rat after focal cerebral ischemia. Brain Res 1489, 104–112. 10.1016/j.brainres.2012.10.017 [PubMed: 23063717]

Zhang L, Li Y, Zhang C, Chopp M, Gosiewska A, Hong K, 2011 Delayed administration of human umbilical tissue-derived cells improved neurological functional recovery in a rodent model of focal ischemia. Stroke 42, 1437–1444. 10.1161/STROKEAHA.110.593129 [PubMed: 21493915]

Zhang L, Yi L, Chopp M, Kramer BC, Romanko M, Gosiewska A, Hong K, 2013 Intravenous administration of human umbilical tissue-derived cells improves neurological function in aged rats after embolic stroke. Cell Transplant 22, 1569–1576. 10.3727/096368912X658674 [PubMed: 23127976]

HIGHLIGHTS

- Oxidative damage is lower in the sublesional white matter with hUTC treatment.
- Perilesional iron accumulation is lower with hUTC treatment.
- Extent of microglial activation is higher in the white matter with hUTC treatment.
- Lesion volume and oxidative damage are associated with iron accumulation.

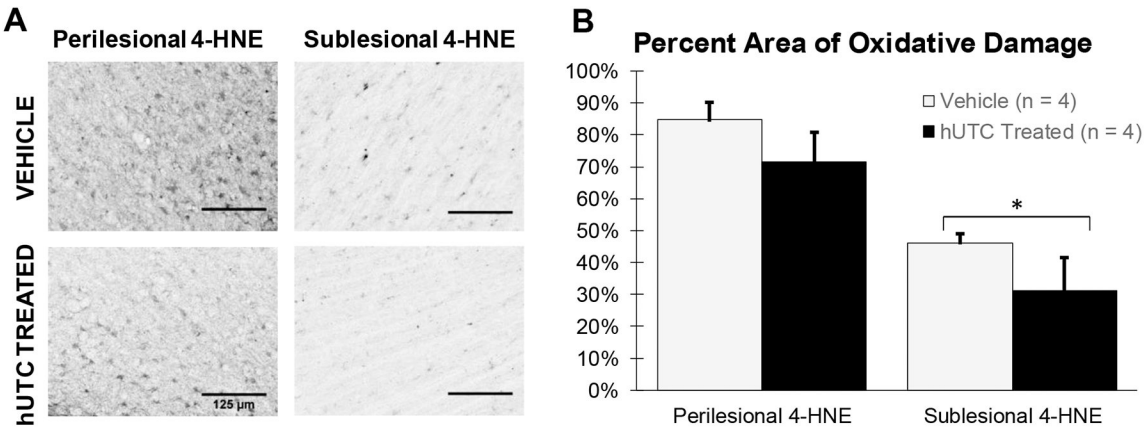

Figure 1: Oxidative damage (4-HNE).

(A) Calibrated micrographs from the ipsilesional hemisphere comparing 4-HNE in perilesional gray matter and sublesional white matter between treatment groups. Scale bar = 125 µm **(B)** 4-HNE staining in the perilesional gray matter did not differ between treatment groups. 4-HNE in the sublesional white matter is lower in the hUTC treated monkeys compared to vehicle controls * $p \leq 0.05$

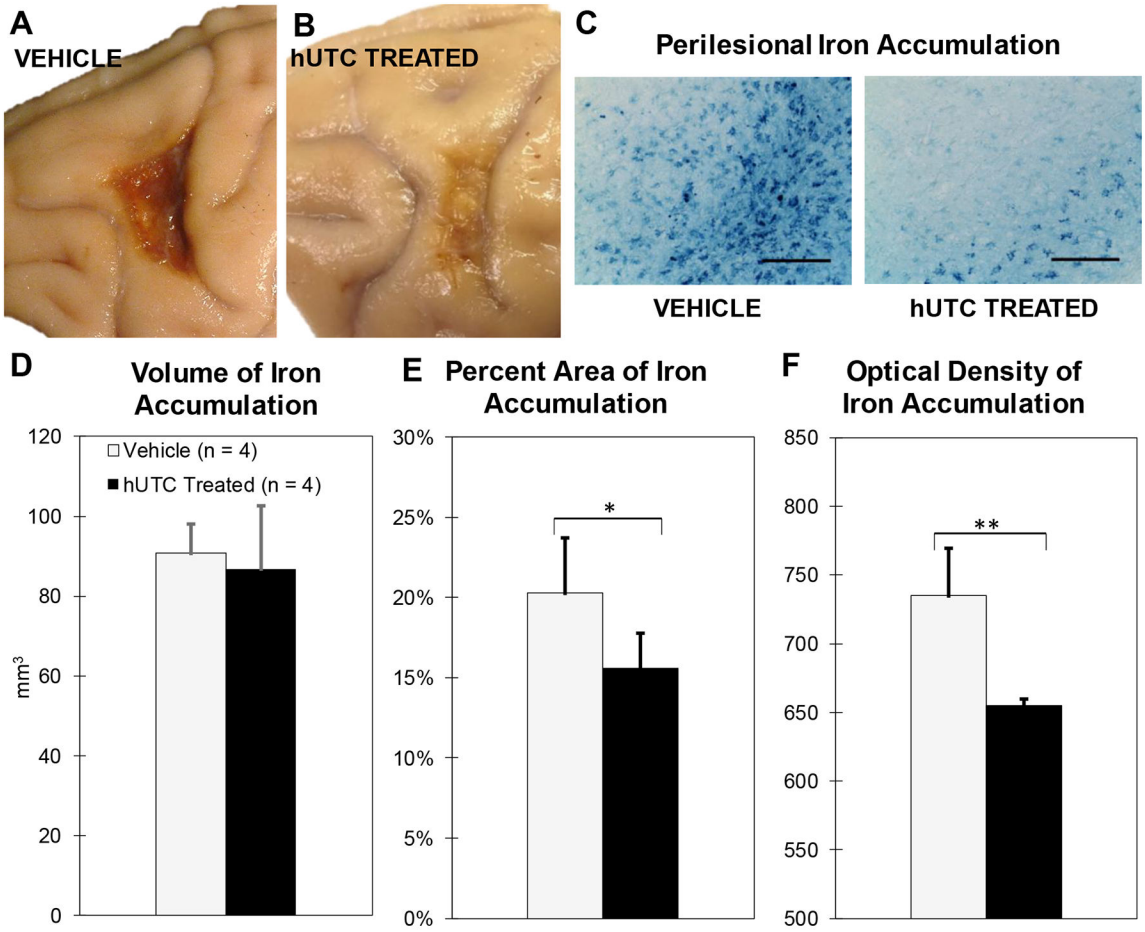

Figure 2: Perilesional Iron Accumulation (Prussian Blue).

(A&B) Calibrated photographs showing differences in lesion appearance in motor cortex 14 weeks post-operatively. **(C)** Calibrated micrographs of iron accumulation in ipsilesional hemisphere comparing both treatment groups. Scale bar = 125 μm **(D)** Total perilesional area occupied by iron does not differ between treatment groups. **(E)** Perilesional iron accumulation percent is lower in the hUTC treated monkeys compared to vehicle controls **(F)** The calibrated color intensity (0–4095) of iron is lower in hUTC treated monkeys compared to vehicle controls. * $p \leq 0.05$ and ** $p \leq 0.005$

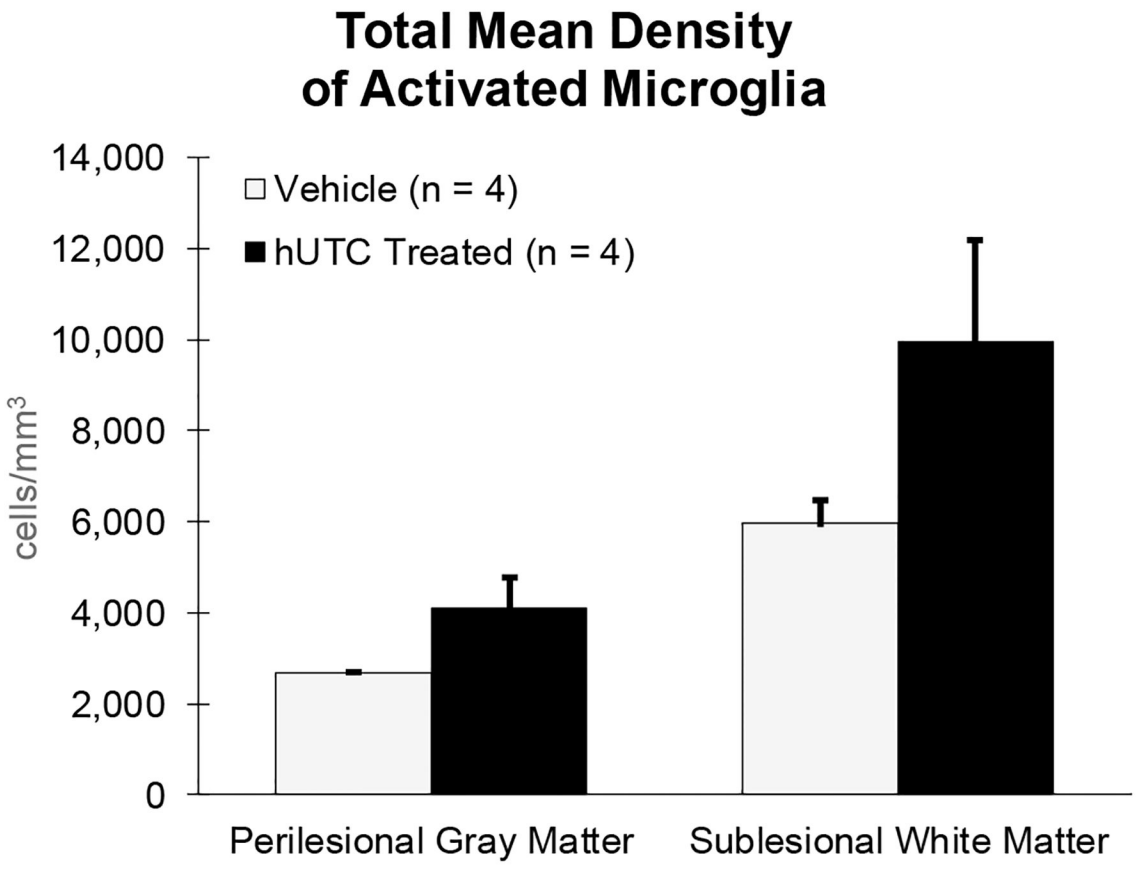

Figure 3: Density of MHC II Activated Microglia.

Density was determined by dividing the estimated cell count from unbiased stereology by the Cavalieri volume estimation. All numbers represent cells/mm^3. Total density of activated microglia did not differ in the perilesional gray matter or sublesional white matter between treatment groups.

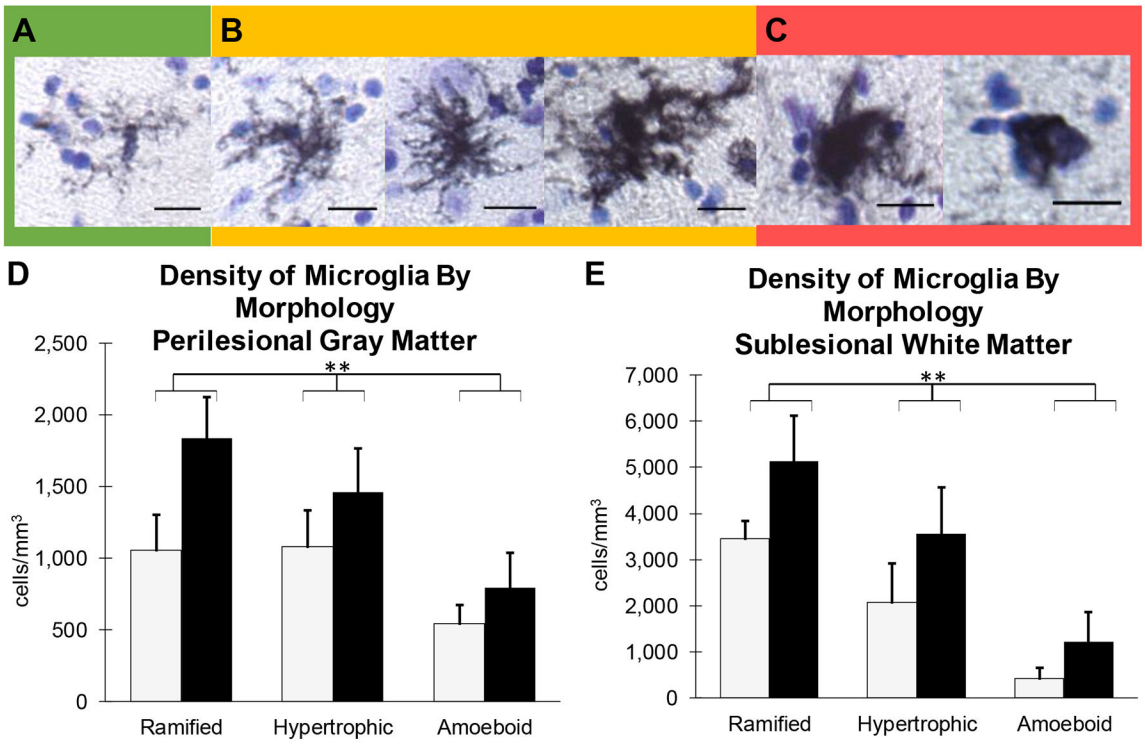

Figure 4: MHC-II Activated Microglia By Morphology.

Representative micrographs of the spectrum of MHC II Activated Microglia morphology observed and quantified. **(A)** Ramified microglia exhibit a small, well-defined cell body and thin processes and were representative of a surveilling phenotype. **(B)** Hypertrophic microglia present with either a small cell body and thick retracted processes or a large cell body with thin processes and represent a transition state of de-ramifying or re-ramifying. **(C)** Amoeboid microglia have thick retracted processes or no processes extending from an enlarged cell body and represent mobile, phagocytic cells. Scale Bar = 25μm. **(D and E)** Density was determined by dividing the estimated cell count from unbiased stereology by the Cavalieri volume estimation. All numbers represent cells/mm^3. When separated by morphology, there was no difference in mean density of activated microglia by morphology in perilesional gray matter **(D)** or sublesional white matter **(E)** by treatment group, but there is a significant difference between cell types ** $p \leq 0.005$

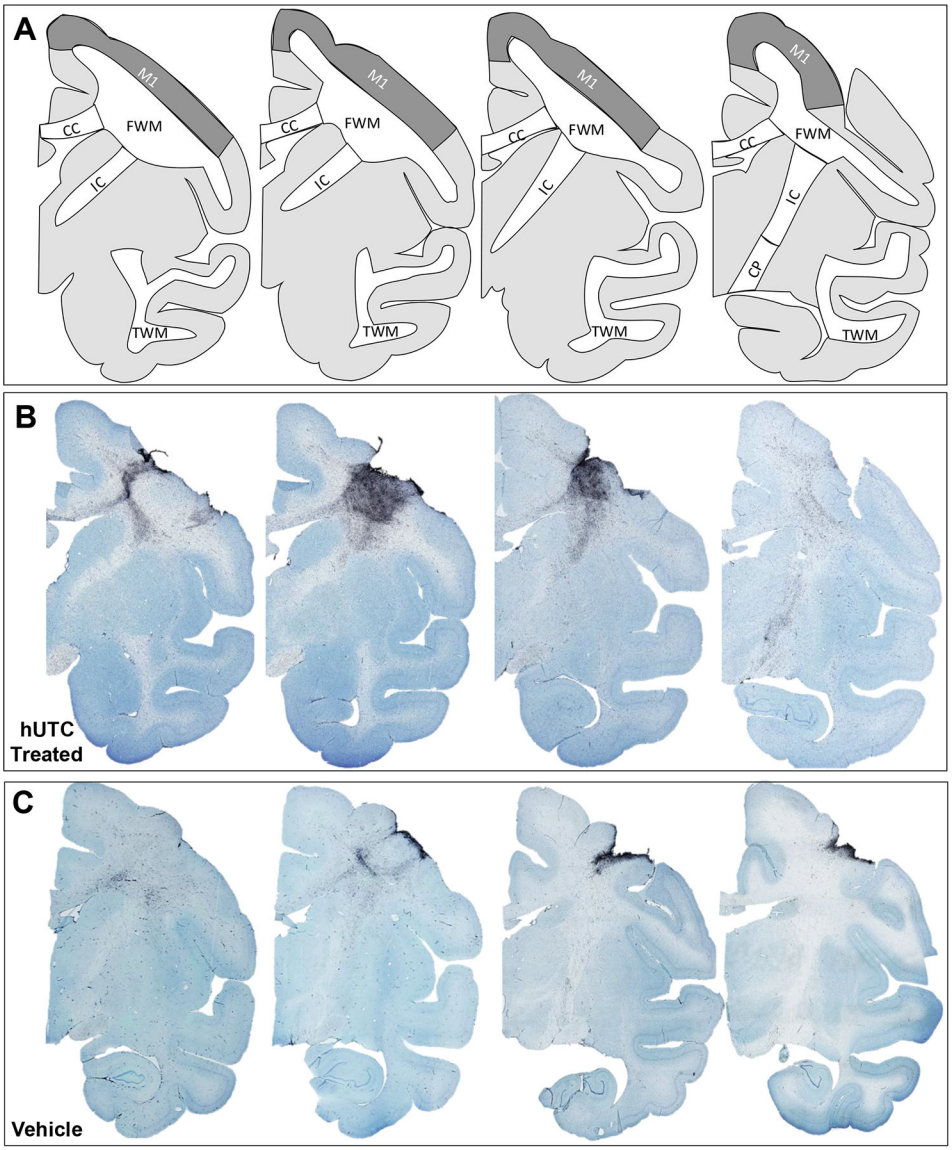

Figure 5: MHC-II Activated Microglia in white matter pathways.

(A) Schematic representations of rhesus monkey coronal sections are shown from rostral to caudal. Relevant regions of interest are outlined. Representative micrographs of thionin stained sections of the lesion hemisphere from rostral to caudal of hUTC treated **(B)** and vehicle treated control **(C)**. Abbreviations: M1 = primary motor cortex; FWM = frontal white matter; CC = corpus callosum; IC = internal capsule; CP = cerebral peduncle; TWM = temporal white matter

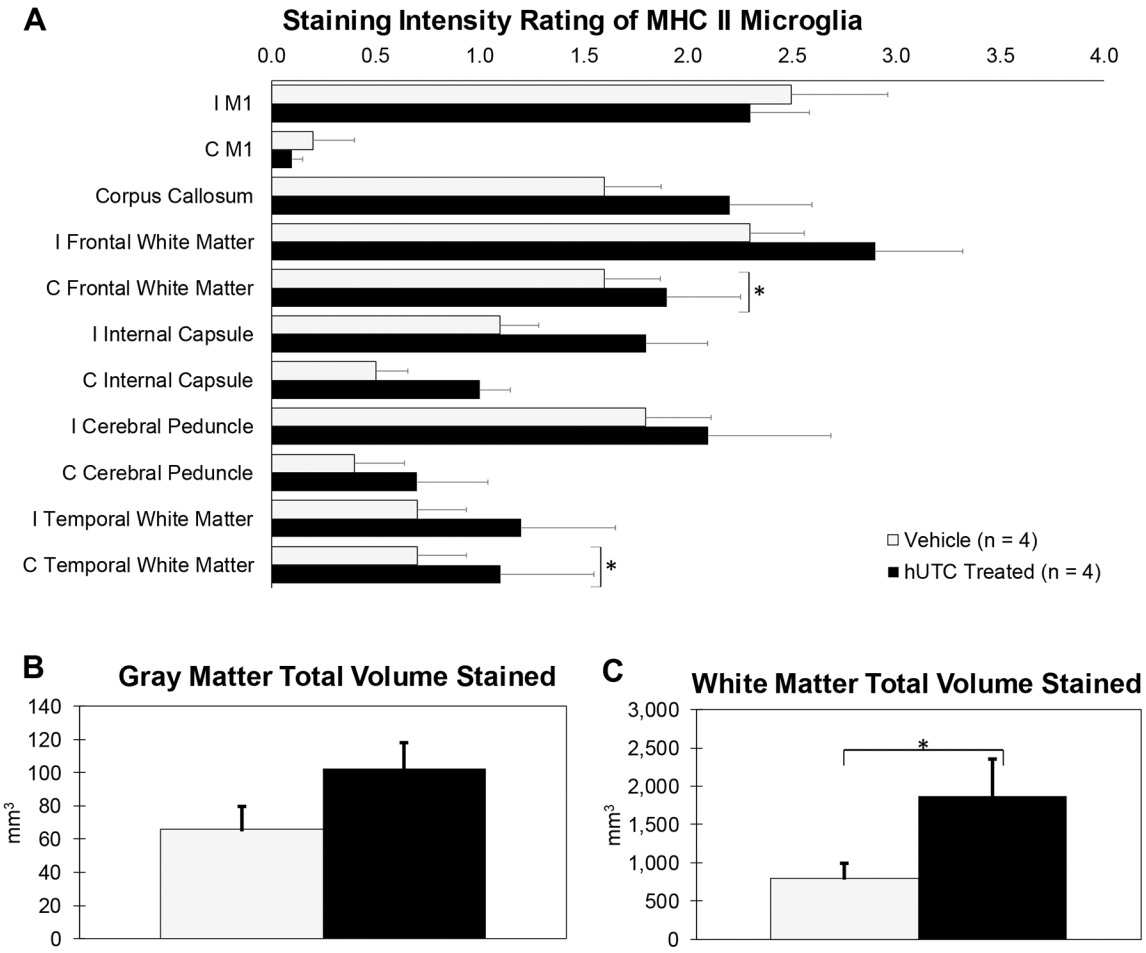

Figure 6: Staining Intensity and Total Area Stained of MHC II Activated Microglia in Gray and White Matter Structures.

Ratings between 0 (no staining) and 4 (intense staining) were given to specific regions. Then, sections with regions scoring 2, 3, or 4 were outlined and the total gray and total white matter areas were measured. **(A)** Staining intensity was significantly higher in contralesional frontal and temporal white matter in hUTC treated monkeys compared to vehicle controls **(B)** There was no difference between gray matter areas stained. **(C)** However, the extent of staining in white matter areas (ipsilesional and contralesional) was significantly higher with hUTC treatment. * $p \leq 0.05$

Abbreviations: I = ipsilesional; C = contralesional; M1 = primary motor cortex

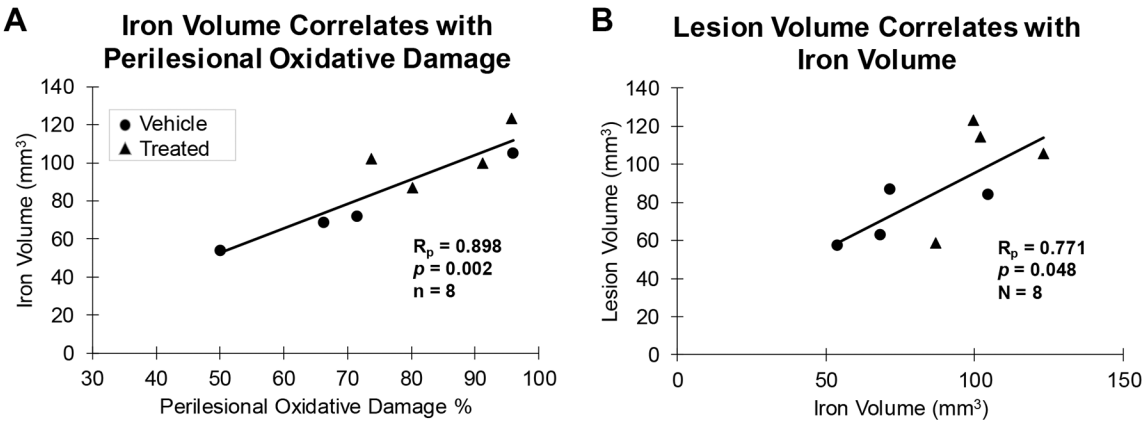

Figure 7: Correlations between markers in the current study and lesion volume.

(A) The volume of the cortex occupied by iron exhibits a positive correlation with oxidative damage (4-HNE) in both perilesional gray matter. **(B)** The volume of the cortex occupied by iron exhibits a positive correlation with the reconstructed lesion volume.

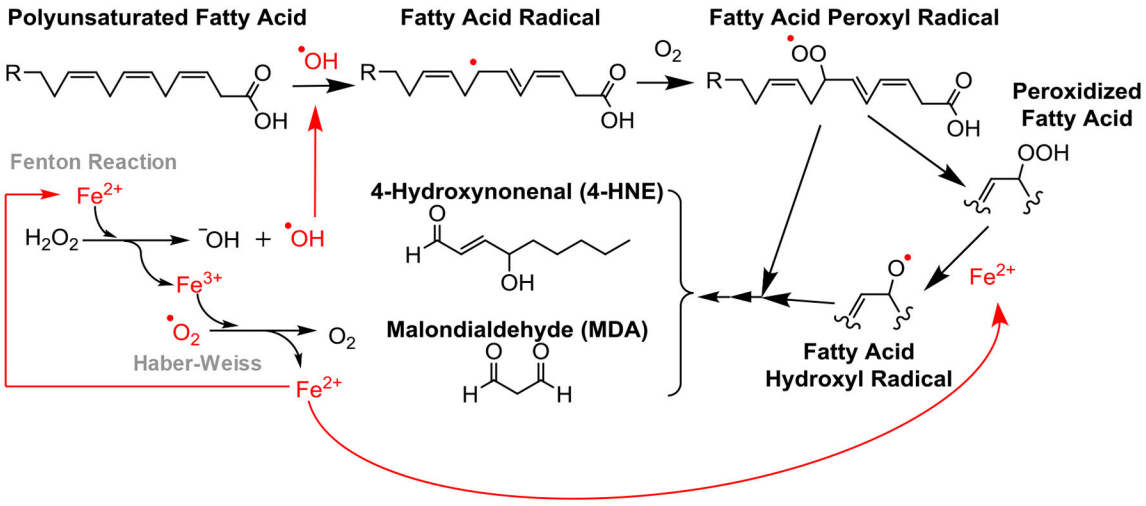

Figure 8: Summary of relevant mechanisms.

Summary of the lipid peroxidation reaction, Fenton reaction, and Haber-Weiss cycle to depict the cyclic nature of free radical formation and iron dysregulation following an ischemic event. Lipid peroxidation to cell membranes results in 4-HNE and MDA accumulations and increases in the presence of ferro us iron and reactive oxygen species.

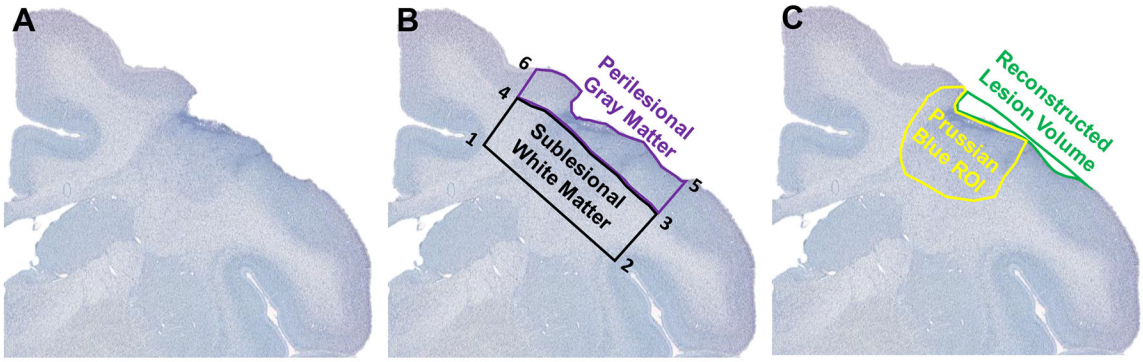

Figure 9: Regions of interest for densitometry and stereology.

One thionin stained sections containing the lesion section is shown here **(A)**. Representations of ROI tracings of Perilesional Gray Matter (PLG) and Sublesional White Matter (SLW) are shown **(B)**. PLG and SLW were ROI used for 4-HNE densitometry and LN3 stereology. PLG and SLW were bounded medially by the depths of the cingulate sulcus (1) and laterally by the depths of the circular sulcus (2). The gray-white boundary separates PLG and SLW (3–4). PLG follows the cortical surface (5–6). Representations of ROI tracings for reconstructed lesion volume and affected cortex are shown **(C)**. The reconstructed lesion volume represents cortex lost and affected cortex represents the area of iron accumulation and gliosis.

Table 1 -

Subject Data.

Subject	Sex	Age (years)	Treatment Group	Lesion Hemisphere	Lesion Volume (mm^3)*	Supplier
SM014j	M	8.5	Placebo	L	87	CPRC
SM018j	M	9.6	Placebo	L	84	CPRC
SM020j	M	9.3	Placebo	R	123	CPRC
SM022j	M	10.6	Placebo	R	59	CPRC
SM016j	M	10.1	hUTC Treated	L	63	CPRC
SM017j	M	8.6	hUTC Treated	L	58	CPRC
SM021j	M	11.5	hUTC Treated	R	114	CPRC
SM024j	M	12.1	hUTC Treated	L	106	YNPRC

Abbreviations: **hUTC**, human umbilical tissue derived cells (CNT00007, Advanced Technologies and Regenerative Medicine, LLC - merged with DePuy Orthopaedics, Inc on 30 December 2012 - Johnson & Johnson, New Brunswick, NJ). **CPRC**, Caribbean Primate Research Center, University of Puerto Rico, San Juan, PR. **YNPRC**, Yerkes National Primate Research Center, Emory University, Atlanta, GA.

*Previously published data in Moore et al., 2013 (used in correlation studies in the current study)